Hygroscopic growth obscures actual variation in anthropogenic aerosol optical depth over central China during 2010-2024

Yun He[1,2,3,*], Dongzhe Jing[1,2,3,*], Zhenping Yin[4], Detlef Müller[4], Fuchao Liu[1,2,3], Yunpeng Zhang[1,2,3], Yang Yi[4], Kaiming Huang[1,2,3], Fan Yi[1,2,3]

5 [1]School of Earth and Space Science and Technology, Wuhan University, Wuhan 430072, China.

[2]State Observatory for Atmospheric Remote Sensing, Wuhan 430072, China.

[3]Key Laboratory of Geospace Environment and Geodesy, Ministry of Education, Wuhan 430072, China

[4]School of Remote Sensing and Information Engineering, Wuhan University, Wuhan 430072, China.

*Correspondence to: Yun He (heyun@whu.edu.cn) and Dongzhe Jing (dz.jing@whu.edu.cn)

10

Abstract. Particle bulk optical property parameters play an essential role in evaluating air quality, however, both parameters can be substantially enhanced under humid atmospheric conditions via hygroscopic growth. Here we use 532-nm polarization lidar observations and ERA5 humidity data during 2010–2024 to retrieve vertical profiles of ambient and dry aerosol backscatter and extinction coefficients of anthropogenic pollution over central China. Particle hygroscopic growth

15 led to enhanced particle backscatter coefficient by 11–46% below 2 km on an annual basis for the considered time frame. Anthropogenic Aerosol Optical Depth (AOD) was 30.7% higher under ambient atmospheric conditions. We found values of $AOD_{amb} = 0.404$ and $AOD_{dry} = 0.309$. During China's rapid air-cleaning period of 2010-2017, AOD_{amb} declined significantly by -0.068 yr^{-1}; in contrast, the rate of decrease of AOD_{dry} was -0.049 yr^{-1} which is 28% slower, but the decrease of the dry aerosols more accurately captures aerosol emission reductions. Hygroscopic-growth-induced net AOD (ΔAOD_{RH})

20 dropped sharply in 2011–2014, most likely as a result of emission mitigation and drier atmospheric conditions, then rebounded in 2014–2019 as rising humidity conditions and the presence of hydrophilic aerosols. Since 2020, ΔAOD_{RH} has remained high attributing to rising humidity conditions but weakening hygroscopicity. While AOD_{amb} suggests peak pollution in summer, AOD_{dry} identifies winter as the true air-pollution maximum. These results highlight the significant impact of aerosol water uptake on its optical properties; therefore, it must be accounted for to ensure accurate air quality

25 assessments.

1 Introduction

Over the past few decades, rapid industrialization and urbanization in China have led to a significant increase in the emission of anthropogenic aerosols, resulting in a major environmental challenge, i.e., atmospheric/air pollution (Che et al., 2007; Wang et al., 2009; Zhang et al., 2012). Episodes of haze events have become more frequent and intense post-2011, posing a serious risk to human health (Li et al., 2023). One of the most widespread, prolonged, and severe haze events occurred in January 2013, affecting vast regions across North, East, Central, and South China with satellite-observed aerosol optical depth (AOD) exceeding 2.0 (Tao et al., 2014; Wang et al., 2014; Zhang et al., 2021). Since then, the issue of atmospheric pollution has received widespread attention.

In response, the Chinese government has implemented a series of air quality control policies since 2013 (The State Council of the People's Republic of China, 2013, 2018, 2023). As a result, significant improvements in air quality have been observed over the past 15 years, as evidenced by large reductions in surface PM2.5 concentrations and AOD, and increased visibility (Zheng et al., 2018; Ding et al., 2019; Zhang et al., 2019; de Leeuw et al., 2022). From 2013 to 2017, surface PM2.5 concentrations rapidly declined by 33% (Zhang et al., 2019); however, the improvement in the frequency of low visibility scenarios has not been as rapid as expected, given the significant reduction in aerosol mass concentration (Liu et al., 2020; Xu et al., 2020). From 2018 onwards, the improvement of air quality has notably slowed down or even stagnated (Geng et al., 2024; Jing et al., 2025a). This slowdown can be attributed to changes in aerosol composition (Yao et al., 2021), an increased fraction of fine-mode particle (Joo et al., 2025), unfavorable meteorological conditions (Wang et al., 2018), climate change (An et al., 2019), and so on. These factors can even be coupled together, resulting in a complicated issue.

One of the most vital inductive factors is the change of aerosol chemistry composition, with an increase in the proportion of nitrate and a decrease in sulfate (An et al., 2019; Liu et al., 2020; Yao et al., 2021). The higher nitrate content enhances the water-uptake capability of aerosols, which increases their extinction efficiency in a humid (ambient) atmosphere, and is denoted as 'hygroscopic growth'. In recent years, the ongoing warming climate may increase the carrying capacity of moisture in the atmosphere (Stoy et al., 2022), which increases aerosol extinction as a result of particle hygroscopic growth (Chen et al., 2019).

In China, meteorological conditions and changes of atmospheric chemistry together contribute to the limited air quality improvement (i.e., the observation that aerosol extinction does not drop as much as one would expect, and vice versa the lower-than-expected increase of atmospheric visibility, atmospheric transmission, and consequently the decrease of aerosol mass concentration) via aerosol hygroscopic growth. For these reasons, it is necessary to quantify the contribution of aerosol hygroscopic growth to air quality (Kallihosur et al., 2024). Furthermore, aerosols emitted near the surface can be lifted into upper layers of the atmosphere from where they can be transported in the free troposphere by various mechanisms, and where humidity conditions can significantly differ from the conditions in the planetary boundary layer.

Therefore, it is crucial to include height-resolved aerosol extinction measurements in observations of the ambient atmosphere, which allows for an improved understanding of the contribution of aerosol hygroscopicity from the different

60 parts of the atmospheric column (Veselovskii et al., 2009; Perez-Ramirez et al., 2021). Lidar measurements provide height-resolved aerosol optical properties such as extinction and backscatter coefficients, and therefore are particularly useful when combined with relative humidity profiles from radiosonde measurements or reanalysis data to evaluate the impact of aerosol hygroscopicity on the atmospheric environment (Granados-Muñoz et al., 2015; Sicard et al., 2022). In addition, aerosol extinction can be used to retrieve visibility (Wu et al., 2016) and aerosol mass concentration (Ganguly et al., 2009; Mamouri

65 and Ansmann, 2016; Shin et al., 2025); these parameters are widely applied in air quality assessment. In this context, correcting the hygroscopic-growth-induced amplification of aerosol extinction in advance is essential to realize valid spatio-temporal comparisons or evaluations of air quality regionally and globally (Toth et al., 2016).

Zhang et al. (2019) observed significant reductions in PM2.5 concentrations across China from 2013 to 2017, with the highest levels of PM2.5 concentrations in northern and central China. However, central China has received relatively less

70 attention compared to other key regions such as the Beijing-Tianjin-Hebei region (BTH), the Yangtze River Delta region (YRD), and the Pearl River Delta region (PRD) (He et al., 2020). Central China hosts massive local industries that contribute to numerous types of anthropogenic aerosol emissions (Zhang et al., 2015; Liao et al., 2020). In particular, central China is located in a subtropical monsoon region that is strongly impacted by abundant water vapor as a result of evaporation of water from numerous regional lakes and rivers, as well as from long-range transport of water vapor from the oceans surrounding

75 China. With respect to the conditions over central China, Xiao et al. (2025) reported the largest water vapor flux of 353.9 kg m-1 s-1 in summer, resulting from the transport of water vapor from the Indian Ocean by the Asian summer monsoon system, and the lowest value of around 100 kg m-1 s-1 in winter, transported from the Arabian Peninsula and its surrounding seas via the southern branch of the westerlies along the southern side of the Tibetan Plateau. This moisture provides favorable conditions for aerosol hygroscopic growth, which contributes to the formation of low-visibility haze events (Ma et al., 2019).

80 Consequently and to better understand the aforementioned observations, we have been conducting continuous ground-based polarization lidar observations in the megacity of Wuhan in central China since 2010. To the best of our knowledge, our research work uses the longest lidar dataset for central China. We began monitoring the height-resolved local tropospheric aerosols in 2010, which is four years earlier than the start of China's official comprehensive surface pollution measurements in 2014(Yin et al., 2021; Jing et al., 2025a). These observations are used to derive aerosol backscatter and

85 extinction profiles in the lower and middle troposphere, as well as AOD. In this study, we applied a height-resolved hygroscopic-growth modification aerosol model to eliminate the impact of ambient humidity, which allows us to assess the long-term variation of 'dry' aerosol extinction and AOD. Our analysis realizes a more accurate examination of the effectiveness of China's air quality control policies in the past 15 years. This article is organized as follows. In Section 2, we provide a brief description of the instruments and data processing methods. Section 3 presents the variations of optical

90 parameters of anthropogenic aerosols with and without hygroscopic-growth enhancement over Wuhan. Section 4 provides a summary and conclusions.

2 Data and Methods

2.1 Polarization Lidar and Data Processing

Our lidar site is located on the campus of Wuhan University (30.5° N, 114.4° E) in Wuhan, China. A 532-nm ground-
based polarization lidar has been used for continuously observing tropospheric aerosols since October 2010 (Kong and Yi,
2015; He et al., 2021; Yi et al., 2021a, 2021b; Jing et al., 2024, 2025a, 2025b). The raw data are stored with a time resolution
of 1 min and a vertical resolution of 30 m. A total of 24910 cloud-free profiles with signal accumulation times of 30-80
minutes were obtained from 2139 days between October 2010 and September 2024 by a cloud screening algorithm (Yin et
al., 2021). For each profile, the particle backscatter (or extinction) coefficient β_p (α_p) is retrieved using the Fernald method
(Fernald, 1984), assuming a fixed lidar ratio of 50 sr. In addition, the lidar provides the linear volume (aerosol + molecule)
and linear particle (only aerosol) depolarization ratios, i.e., δ_v and δ_p. These two parameters indicate the degree of the non-
sphericity of the scattering objects (Freudenthaler et al., 2009). Based on β_p and δ_p, we can derive the dust and non-dust
component of the particle backscatter (extinction) coefficient β_d and β_{nd} (α_d and α_{nd}) using the polarization-lidar
photometer networking (POLIPHON) method (Tesche et al., 2009; Mamouri and Ansmann, 2014). In Wuhan, the non-dust
component is primarily associated with anthropogenic aerosols.

2.2 Radiosonde and ERA5 Reanalysis Data

Two radiosondes are launched daily around 0800 and 2000 local time (LT) at 30.6° N, 114.1° E, approximately 24 km
away from our lidar site. The radiosondes provide us with vertical profiles of temperature, pressure, relative humidity (RH),
water vapor mixing ratio (WVMR), wind speed (WS), and wind direction (WD) from the surface up to ~30 km altitude.
Potential temperature θ is calculated from these meteorological parameters with the method by Bolton (1980). To match the
altitude bins of lidar profiles, radiosonde data with variable vertical resolution are interpolated using a cubic spline
interpolation method. The matched radiosonde and lidar profiles are then used to identify aerosol hygroscopic growth cases
and estimate the associated hygroscopic growth parameter γ.

The European Center for Medium-Range Weather Forecasts (ECMWF) fifth-generation reanalysis (ERA5) provides
global hourly atmospheric data from January 1940 onward (Copernicus Climate Change Service, Climate Data Store, 2025).
ERA5 RH profiles (Hersbach et al., 2023a) are interpolated to match the altitude bins of lidar profiles and used to assess the
influence of hygroscopic growth on the particle backscatter coefficient. Figure 1 shows the differences in RH data obtained
from radiosonde measurements and ERA5 data over Wuhan. The comparably small mean difference of -0.63% suggests that
it is reasonable to use ERA5 RH data for the long-term study. ERA5 boundary layer height (BLH) data are also applied to
distinguish hygroscopic growth effects within the boundary layer (BL) and free troposphere (FT) (Hersbach et al., 2023b).
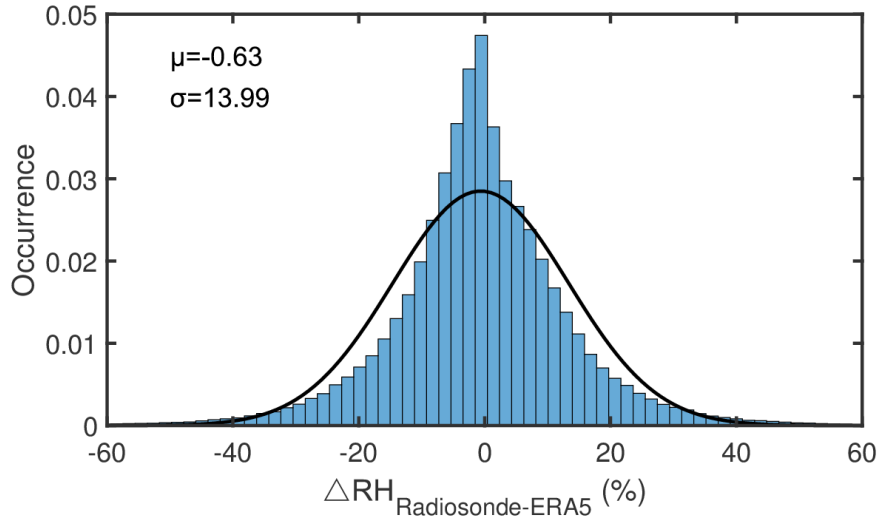The diurnal maximum BLH is adopted as the boundary between the BL and FT.

Figure 1. The differences in RH over Wuhan between 2010 and 2024 obtained from simultaneous radiosonde measurements and ERA5 data. μ is the mean value and σ is the standard deviation.

125

2.3 Dry Aerosol Optical Depth Estimation

The capability of lidar to measure aerosol hygroscopicity was first demonstrated by Ferrare et al. (1998). Subsequently, a thorough method of quantitatively estimating the aerosol hygroscopic properties based on lidar observations was established by Veselovskii et al. (2009). In this study, the variation of the lidar-derived anthropogenic particle backscatter coefficient

130 β_{nd} with RH is considered under the assumption of an external mixture between dust and non-dust (anthropogenic) aerosols (Jing et al., 2025b). The particle backscatter coefficient enhancement factor, $f_\beta(RH)$, is defined as the ratio of β_{nd} at a given RH to that for dry conditions (Hänel, 1976):

$$f_\beta(RH) = \frac{\beta_{nd}(RH)}{\beta_{nd}(RH_{dry})} \tag{1}$$

Lidar-derived cloud-free profiles within 2 hours before or after radiosonde launches (around 0800 or 2000 LT) are

135 selected. An aerosol layer is identified, when β_{nd} increases monotonically and simultaneously with radiosonde-measured RH. Within such aerosol layers, variations of key radiosonde meteorological parameters are constrained as follows: (1) $\triangle$WVMR < 2 g·kg⁻¹; (2) $\triangle\theta$ < 2 K; (3) $\triangle$WS < 2 m·s⁻¹; (4) $\triangle$WD <15° (Sicard et al., 2022). These criteria indicate well-mixed atmospheric conditions and ensure that the observed increase in β_{nd} is driven solely by water uptake rather than additional aerosol emissions or compositional changes (Granados-Muñoz et al., 2015). Since the RH range varies among different cases,

140 a common reference RH_{ref} is required for comparability. Accordingly, the widely used Hänel parameterization is applied to obtain the reference backscatter enhancement factor, $f_{ref-Hänel}(RH)$ (Veselovskii et al., 2009; Perez-Ramirez et al., 2021):

5

$$f_{\text{ref-Hänel}}(RH) = \left(\frac{1 - \frac{RH}{100}}{1 - \frac{RH_{\text{ref}}}{100}}\right)^{-\gamma} \tag{2}$$

where γ is the hygroscopic growth parameter, with small values representing weakly hygroscopic particles (e.g., dust) and large values representing highly hygroscopic particles (e.g., sea salt) (Titos et al., 2016). In this study, we adopt $RH_{\text{ref}} =$ 40%, a threshold commonly used to define the upper limit of the initial dry conditions (Granados-Muñoz et al., 2015; Navas-Guzmán et al., 2019; Sicard et al., 2022). Combining Equations (1) and (2), the dry backscatter coefficient of anthropogenic aerosols can be expressed as:

$$\beta_{\text{nd,dry}} = \frac{\beta_{\text{nd}}(RH)}{f_{\text{ref-Hänel}}(RH)} = \begin{cases} \beta_{\text{nd}}(RH)/\left(\frac{1 - \frac{RH}{100}}{1 - \frac{RH_{\text{ref}}}{100}}\right)^{-\gamma} & RH \geq 40\% \\ \beta_{\text{nd}}(RH) & RH < 40\% \end{cases} \tag{3}$$

Due to the lack of a Raman channel in our lidar system, the hygroscopic effect on lidar ratio is not considered in this study (Zhao et al., 2017). The dry particle extinction coefficient $\alpha_{\text{nd,dry}}$ can be obtained by multiplying $\beta_{\text{nd,dry}}$ with a fixed lidar ratio of 50 sr. Thus, the ambient aerosol optical depth (AOD_{amb}) and dry aerosol optical depth (AOD_{dry}) for anthropogenic aerosols can be given by:

$$AOD_{\text{amb}} = \int_{Z_b}^{Z_t} \alpha_{\text{nd}}(z)\text{d}z \tag{4}$$

$$AOD_{\text{dry}} = \int_{Z_b}^{Z_t} \alpha_{\text{nd,dry}}(z)\text{d}z \tag{5}$$

where Z_b=0 km and Z_t=7 km are the lower and upper integration limits, respectively. The effect of hygroscopic growth on AOD is then defined as (Kallihosur et al., 2024):

$$\Delta AOD_{\text{RH}} = AOD_{\text{amb}} - AOD_{\text{dry}} \tag{6}$$

Furthermore, ΔAOD_{RH} can be divided into contributions from the BL and FT, denoted as $\Delta AOD_{\text{RH,BL}}$ and $\Delta AOD_{\text{RH,FT}}$, respectively. Figure 2 provides the flowchart of the data processing procedure used in this study.
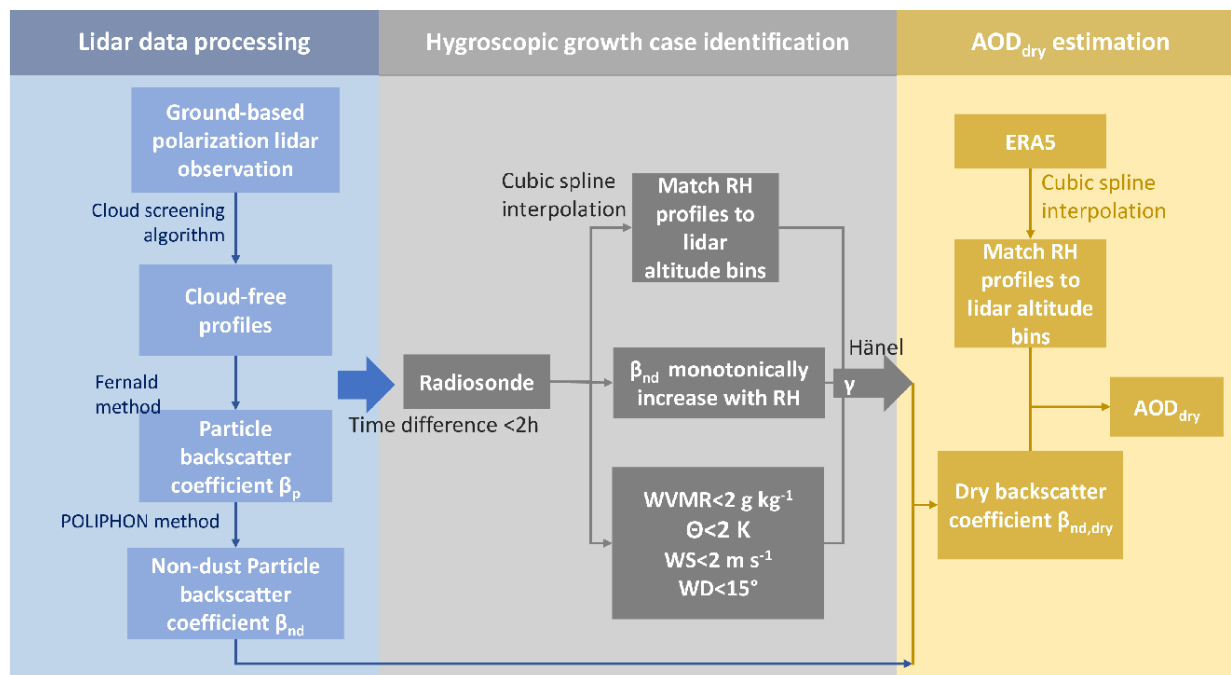
Figure 2. Flowchart of lidar data processing, hygroscopic growth case identification, and the scheme of estimating AOD_{dry} from lidar-derived AOD_{amb}.
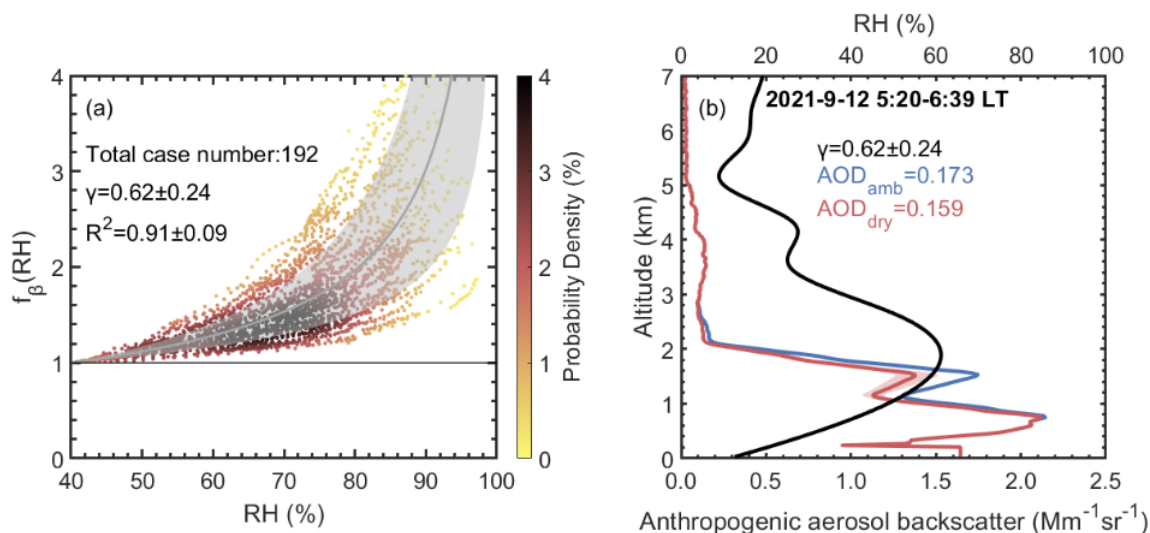
3 Results

3.1 Hygroscopic-Growth-Enhanced Optical Parameters of Anthropogenic Aerosols

165   We examined all the observational data collected with a 532-nm polarization lidar from October 2010 to September 2024. We identified 24910 cloud-free profiles for further analysis. For each cloud-free profile, the particle backscatter coefficient (β_p) profile was derived with an automatic algorithm originally developed by Yin et al. (2021) and later extended by He et al. (2024) and Jing et al. (2025a). Together with particle depolarization ratio (δ_p), the β_p profiles can be divided into dust (β_d) and non-dust (β_{nd}) backscatter coefficient profiles (Mamouri and Ansmann, 2014). The hygroscopic growth of mineral dust

170   was neglected due to its hydrophobic nature. The influence of sea salt was negligible since Wuhan is an inland city (He et al., 2025). All the non-dust components were considered anthropogenic aerosols. We identified 192 cases (cloud-free aerosol profiles) with specific features regarding anthropogenic aerosol hygroscopic growth (see method section for details). The particle backscatter coefficient-related enhancement factor, $f_\beta(RH)$, is shown by the blue curve in Figure 3a. Using the Hänel parameterization (Hänel, 1976), we derived a corresponding hygroscopic growth parameter $\gamma = 0.62 \pm 0.24$. For

175   urban pollutions, γ values typically situate between 0.4 and 0.6, depending on the proportions of inorganic salt components,

such as sulfate and nitrate, which are generally considered more hydrophilic (Bedoya-Velásquez et al., 2018; Sicard et al., 2022; Miri et al., 2024).

Figure 3b shows a representative example on 12 September 2021, along with the relative humidity (RH) profile from EAR5 reanalysis data. The criteria for identifying such an aerosol hygroscopic growth case are introduced in detail in the

180 method section hereafter. Concurrent observations of the volume (particle + molecule) depolarization ratio also indicate the anthropogenic (non-dust) aerosols during the period (not shown here). During 0520-0639 LT (Local Time), the lidar-derived particle backscatter coefficient in the ambient atmosphere was clearly enhanced by aerosol hygroscopic growth at altitudes of 1-2 km, where RH exceeded 40% (Sicard et al., 2022). By integrating the particle backscatter coefficient from surface to 7-km altitude and assuming a fixed lidar ratio of 50 sr (Fernald, 1984), the 532-nm AOD changed from 0.173 (AOD_{amb}) to

185 0.159 ± 0.005 (AOD_{dry}), indicating an AOD increase of approximately 9% due to hygroscopic growth. In addition, Jing et al. (2025b) observed a year-by-year variation of γ values over Wuhan. These variations were caused by changes of the chemical compositions of anthropogenic aerosols. In our study, we used the annual mean of γ for each year (Jing et al., 2025b), respectively, for calculating the lidar-derived particle backscatter coefficient under dry and humid ambient atmospheric conditions.

190

Figure 3. (a) Probability density distribution of particle backscatter coefficient enhancement factors ($RH_{ref} = 40\%$) from 192 identified anthropogenic aerosol hygroscopic growth cases in the lower and middle troposphere (0-7 km); (b) Example of modifying a lidar-derived ambient particle backscatter coefficient profile (blue curve) to a dry profile (red curve) by removing the hygroscopic growth contribution on 12 September 2021. The red shaded area represents

195 **the uncertainty based on the standard deviation of γ (0.24). The RH profile (black curve) is provided by ERA5 reanalysis data.**
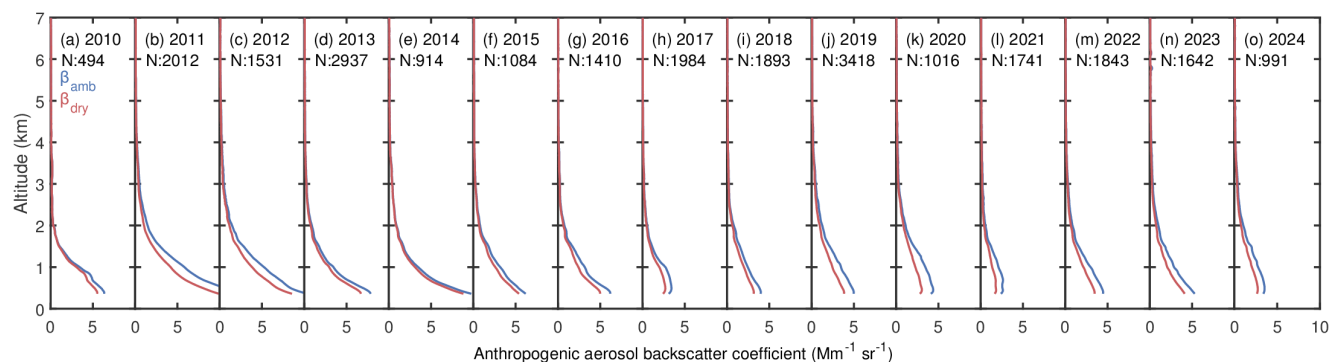
Figure 4. Annual mean profiles of lidar-derived 532-nm anthropogenic aerosol backscatter coefficient under ambient and dry conditions over Wuhan, i.e., $\beta_{nd,amb}$ and $\beta_{nd,dry}$. 'N' denotes the number of profiles used for calculating the average profile for each year.

Figure 4 presents the annual mean profiles of the anthropogenic aerosol backscatter coefficient derived under ambient and dry atmospheric conditions, i.e., $\beta_{nd,amb}$ and $\beta_{nd,dry}$. It can be seen that aerosol hygroscopic growth mainly takes place in the lower troposphere (from the surface to ~3km). In particular, below 2 km, the particle backscatter coefficient is enhanced by 11-46 % due to hygroscopic growth. With the substantial improvement of air quality in China, $\beta_{nd,amb}$ values within the lower troposphere have generally decreased.

All the lidar-derived particle backscatter coefficient profiles were modified from ambient to dry atmospheric conditions by the use of the pre-derived annual mean hygroscopic growth parameter. On the basis of this information, we obtained AOD_{amb} and AOD_{dry} for the anthropogenic aerosols (see method section for details). Figure 5 presents the frequency distribution of AOD_{amb} and AOD_{dry} in Wuhan. The mean values of AOD_{dry} and AOD_{amb} were 0.309 and 0.404, respectively, across the period considered in our study. These values suggest that hygroscopic growth on average increased AOD by 30.7% under humid atmospheric conditions. This change of AOD corresponds to an extinction enhancement factor (AOD_{amb}/AOD_{dry}) of 1.31, which is much lower than the value of approximately 1.8 reported for India (Nair et al., 2020; Kallihosur et al., 2024). Notably, the frequency distribution patterns of AOD_{dry} and AOD_{amb} are rather different. AOD_{amb} shows a slightly skewed, relatively broad Gamma distribution with a peak around 0.30-0.50, whereas AOD_{dry} exhibits a much narrower Gaussian distribution with a sharp maximum at 0.30-0.35. After accounting for hygroscopic growth, most AOD values exceeding 0.70 disappear, suggesting that hygroscopic growth largely increased the occurrence of severe air pollution events in Wuhan (Zhang et al., 2021). A similar changing pattern was reported by Kallihosur et al. (2024) for the hygroscopic modification of AOD over the eastern Indo-Gangetic Plain using satellite observations. The only major difference is that AOD_{amb} in India exhibited a much higher peak close to 0.5 of the frequency distribution. This result points to a higher content of water vapor in the atmosphere, which thereby leads to stronger particle hygroscopic growth.
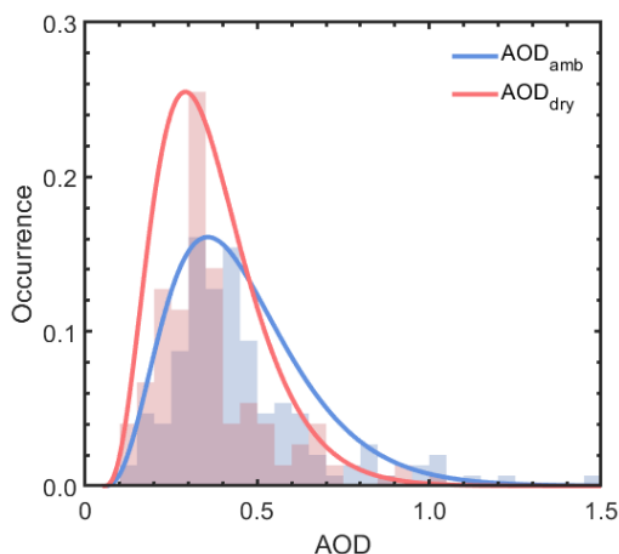
Figure 5. Frequency probability of the lidar-derived 532-nm anthropogenic (non-dust) AOD_{amb} and AOD_{dry} in Wuhan during 2010-2024.

3.2 Long-Term Variation of Anthropogenic AOD in the Ambient and Dry Atmosphere

225   Figure 6a illustrates the evolution of lidar-derived anthropogenic AOD_{amb} and AOD_{dry} in Wuhan from 2011 to 2024. For representativeness, we removed the value of 2010 from our analysis since the routine observations started only from October of that year. Hygroscopic growth corrections were applied to all cloud-free lidar profiles with the use of EAR5 RH profiles. Jing et al. (2025a) previously reported that the 532-nm AOD_{amb} in Wuhan decreased rapidly with a rate of -0.068 yr^{-1} during 2010-2017 (defined as 'stage I'), followed by a fluctuating period from 2018 to 2024 (defined as 'stage II'). When

230   accounting for hygroscopic growth in 'stage I', the rate of decline of AOD_{dry} was -0.049 yr^{-1}, i.e., approximately 28% lower than the rate of decline of AOD_{amb}. This result indicates that the actual reduction in aerosol emissions was slower than that suggested by the direct lidar measurements in the ambient atmosphere. In contrast, in 'stage II', both AOD_{dry} and AOD_{amb} ceased to decline and instead exhibited slight fluctuations; such a fluctuation pattern of AOD variation after 2017 onwards was also confirmed by MODIS Multi-Angle Implementation of Atmospheric Correction (MAIAC) data across China (de

235   Leeuw et al., 2022). One explanation may be the imbalance in NO_2 and SO_2 emissions, which increases the ability of aerosol water uptake, i.e., aerosol hygroscopicity. This effect is likely to be the reason for offsetting the partial benefits of air pollution mitigation actions (Liu et al., 2018; Geng et al., 2024; Jing et al., 2025a). A marked decrease in both AOD_{amb} and AOD_{dry} occurred in 2020, corresponding to the COVID-19 lockdown (Yao et al., 2021). The subsequent gradual increase reflects the resumption of labor and production processes. Overall, AOD_{dry} provides a more accurate representation of actual

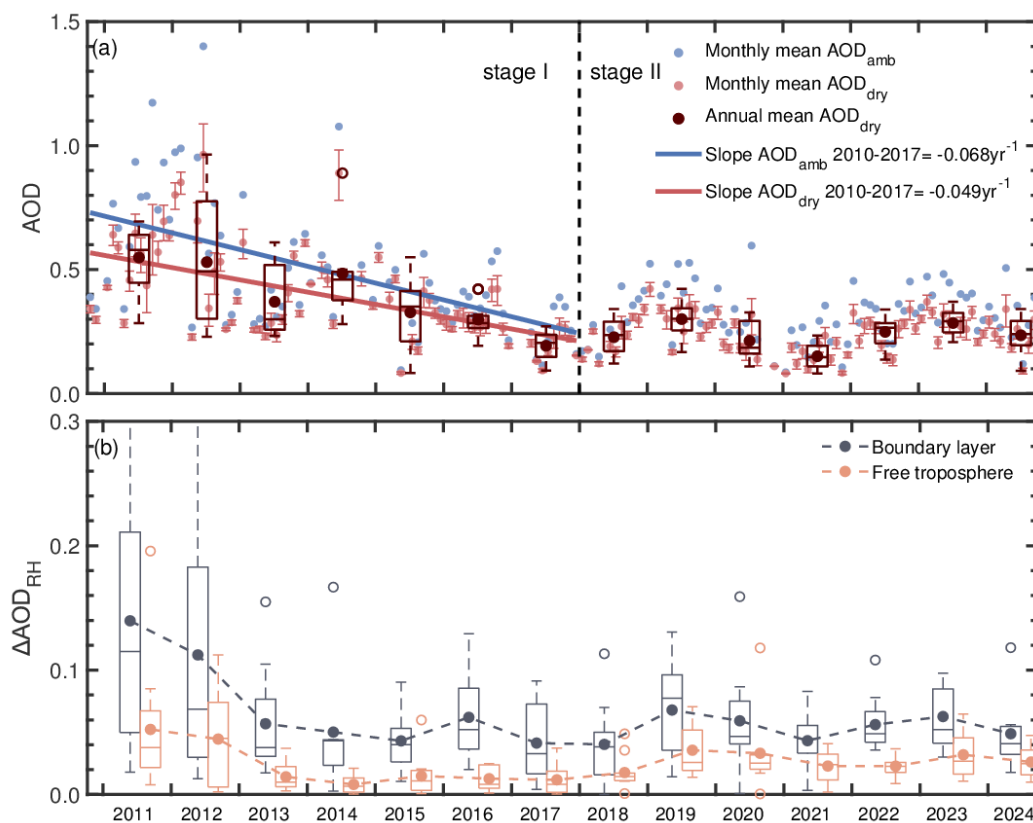240   aerosol emissions than AOD_{amb}.

10

Figure 6. (a) Evolution of lidar-derived anthropogenic AOD$_{amb}$ and AOD$_{dry}$ in Wuhan from 2011 to 2024. Each point denotes a monthly mean value. The error bars on the red points reflect the uncertainties caused by the standard deviation in γ. Linear regressions for 2010-2017 are shown as solid lines. The vertical dashed line divides the data record into stage I (2010-2017) and stage II (2018-2024), as discussed by Jing et al. (2025a). (b) Evolution of enhanced AOD due to hygroscopic growth in the boundary layer and free troposphere, denoted as ΔAOD$_{RH,BL}$ and ΔAOD$_{RH,FT}$, over the same period.

Lidar provides height-resolved measurements of particle extinction, which allows for further analysis of the contributions of hygroscopic growth to AOD in the boundary layer (BL) and free troposphere (FT), denoted as ΔAOD$_{RH,BL}$ and ΔAOD$_{RH,FT}$, respectively, with their temporal evolutions shown in Figure 6b. On an annual basis, ΔAOD$_{RH,BL}$ is generally 2-5 times larger than the corresponding ΔAOD$_{RH,FT}$, indicating a much stronger contribution of aerosol hygroscopic growth within the BL, where most water vapor resides. Both ΔAOD$_{RH,BL}$ and ΔAOD$_{RH,FT}$ exhibit an evident drop between 2011 and 2013, which likely shows the effect of the reduced rate of decline of AOD during 'stage I' (from -0.068 yr^{-1} for AOD$_{amb}$ to -0.049 yr^{-1} for AOD$_{dry}$). During the winter seasons of 2011-2013, comparably high monthly-mean AOD$_{amb}$ values were observed, corresponding to the most severe wintertime haze events recorded in Wuhan (Zhang et al., 2021). These events typically

occurred under conditions of intense aerosol emissions combined with a stagnant and highly humid atmosphere. Such rather severe air pollution episodes were effectively mitigated within the first two years after data collection had begun (2011 and 2012), probably because of the implementation of measures outlined in the '*Technical guidelines for air pollution control projects*' by the Chinese government (Ministry of Ecology and Environment of the People's Republic of China, 2010). From 260   2014 to 2024, $\Delta AOD_{RH,BL}$ is generally stable and only slightly fluctuates between 0.04 and 0.07 with a variation rate lower than 0.002 yr^{-1}. In contrast, $\Delta AOD_{RH,FT}$ has a comparably lower rate of variation between 0 and 0.02 in 2014-2018, after which the variation rate increases to 0.02-0.04 in 2019-2024. This result suggests a more pronounced impact of hygroscopic growth on AOD_{amb} in the FT in recent years.
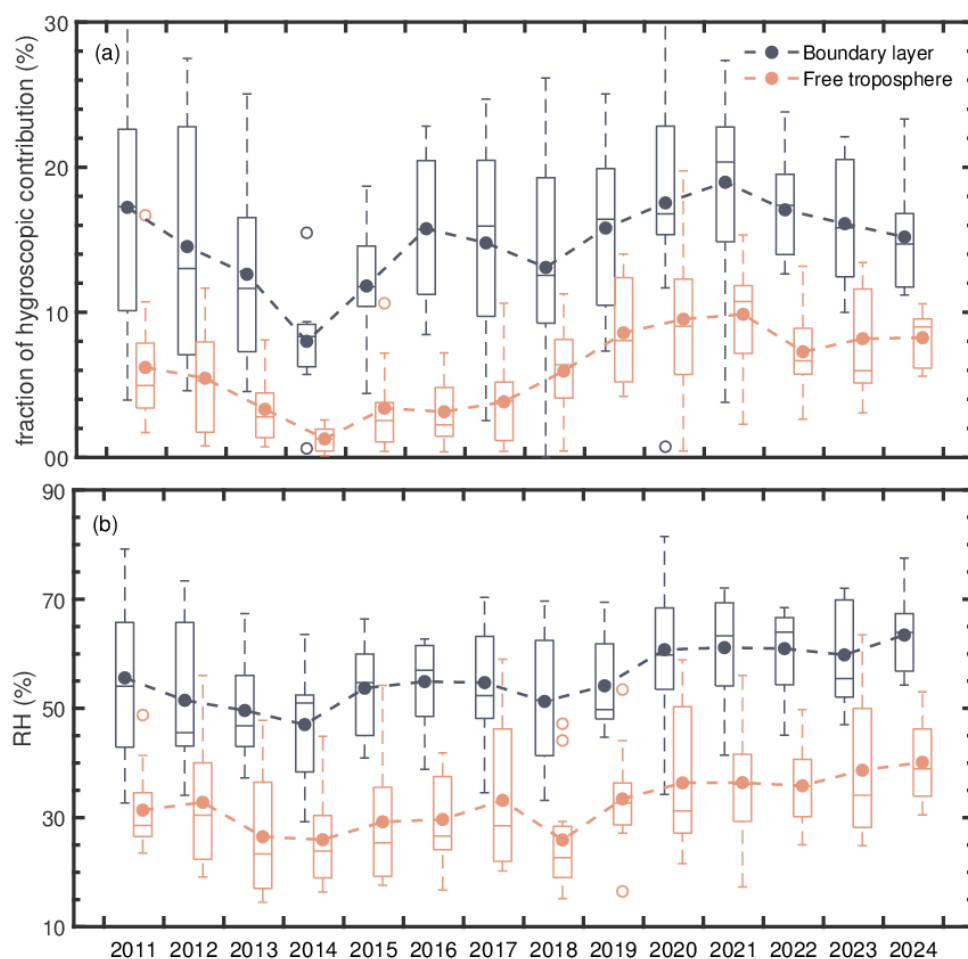

265   **Figure 7. (a) Variation of the fractions of enhanced 532-nm anthropogenic AOD due to hygroscopic growth in the BL and FT, i.e., $\Delta AOD_{RH,BL}/AOD_{amb}$ and $\Delta AOD_{RH,FT}/AOD_{amb}$, from 2011 to 2024. (b) Evolution of the ERA5 RH in the BL and FT over the same period.**

To assess the relative contributions of hygroscopic growth in the BL and FT, Figure 7a presents the annual mean fractions, i.e., $\Delta AOD_{RH,BL}/AOD_{amb}$ and $\Delta AOD_{RH,FT}/AOD_{amb}$, respectively. Figure 7b provides the corresponding RH values in the BL

270   and FT, revealing that the BL (55.8±11.1%) is substantially more humid than the FT (32.7±11.2%). In general, the relative contribution of hygroscopic growth does not vary linearly or monotonously with RH, as it is jointly controlled by aerosol hygroscopicity capability (depends on chemical composition) and ambient moisture conditions. During the initial four-year period (2011-2014), both $\Delta AOD_{RH,BL}/AOD_{amb}$ and $\Delta AOD_{RH,FT}/AOD_{amb}$ show a marked decline, which was driven primarily by effective mitigation of severe air pollution episodes (Jing et al., 2025a) and a concurrent shift toward a drier atmosphere.

275   In general, the atmosphere has become more humid post-2014, with a rate of increase of around 1.3% yr^{-1}, which likely is linked to frequent El Niño events over the past decade, i.e., 2015/16, 2018/19, and 2023/24 (Zhai et al., 2016; Guan et al., 2023; Li et al., 2023). Zhong et al. (2023) reported that El Niño-induced North Pacific anticyclones tend to transport warmer and wetter air to southern China, resulting in increased rainfall and water vapor content. Note that the only exception to the humidifying trend is the dip in RH observed in 2018, which is attributed to the anomalous severe drought that occurred over

280   central China from mid-summer through late autumn, during which year-on-year precipitation declined by 20-50%. However, variations in the fractional contribution of hygroscopic growth can be divided into two periods with distinct patterns. From 2014 to 2019, both $\Delta AOD_{RH,BL}/AOD_{amb}$ and $\Delta AOD_{RH,FT}/AOD_{amb}$ exhibit a gradual increase, rising from 8% to 16% and from 1% to 9%, respectively. This increase is jointly driven by rising RH and a growing proportion of more hydrophilic nitrate aerosols (Jing et al., 2025b). This consistent increasing trend also suggests that aerosol sources and/or compositions in

285   the BL and FT were similar. From 2020 onwards, $\Delta AOD_{RH,BL}/AOD_{amb}$ and $\Delta AOD_{RH,FT}/AOD_{amb}$ fluctuate at relatively high levels of 15-19% and 7-10%, respectively. Although RH continues to increase, the upward trend in the hygroscopic growth contribution is partially offset by a slight decline of the hygroscopic growth parameter γ since 2020 (Jing et al., 2025b).
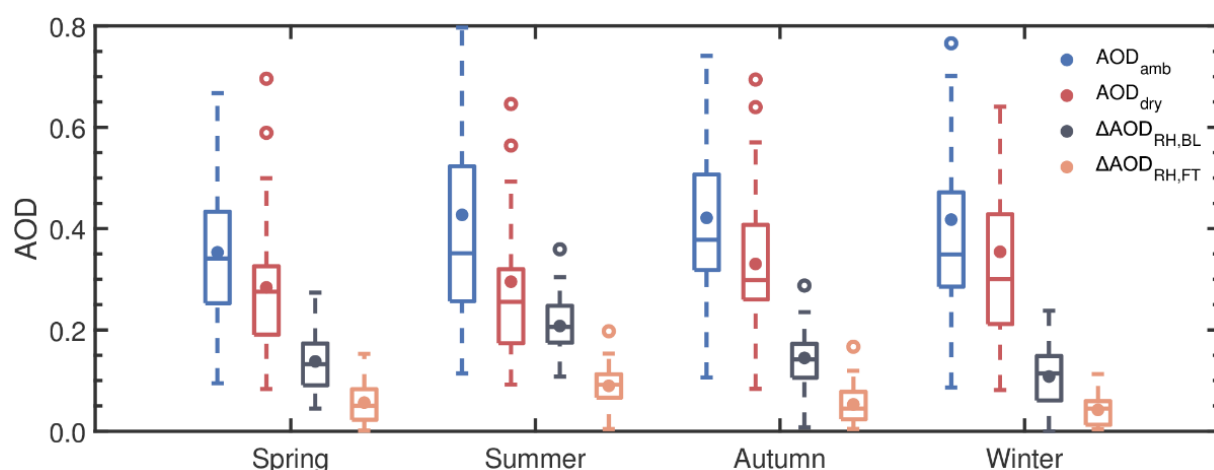
3.3 Seasonal Patterns of Hygroscopic-Growth Contributions to Anthropogenic AOD

Figure 8 shows the seasonal variations of AOD_{amb}, AOD_{dry}, $\Delta AOD_{RH,BL}$, and $\Delta AOD_{RH,FT}$. Based on AOD_{amb}, summer

290   (0.427) appears to be the most polluted season over central China, followed by autumn (0.421) and winter (0.417). However, when examining AOD_{dry}, a different seasonal pattern emerges once hygroscopic growth is considered. The most severe air pollution prevails in winter. We find a maximum value of 0.354 for AOD_{dry}, followed by autumn (0.330) and summer (0.295). This variation of AOD during the seasons reflects a more realistic depiction of air quality over central China, because winter not only holds the highest aerosol emissions (Zhang et al., 2015), but also features stagnant meteorological

295   conditions that hinder the removal of accumulated aerosols from the atmospheric column (Ma et al., 2019; Zhang et al., 2021).

Wuhan is subject to the monsoon climate. The Asian summer monsoon plays an essential role in transporting water vapor from the Indian Ocean and Western Pacific and has a dominant impact on summer precipitation southeast of the Hu Huanyong Line, a line directly connects Heihe in Southwestern China and Tengchong in Northeastern China and generally

300 overlap with the 400-mm isohyet (Zheng et al., 2022). Water vapor over the Yangtze River Valley primarily originates from the Indian Ocean. This water vapor is carried by advection transport associated with the Indian summer monsoon and the West Pacific Subtropical High (Chu et al., 2021). In contrast, the Asian winter monsoon, which is driven by the Arctic Oscillation and Siberian High, advects cold, dry air from Siberia (Wu and Wang, 2002). This movement of air suppresses precipitation in the mid-latitudes of East Asia and therefore results in a relatively cold and dry atmosphere (Wang et al.,

305 2014). These seasonal climatic characteristics lead to much higher atmospheric moisture in summer compared with winter, causing hygroscopic growth to contribute much more to the observed ambient AOD during summer. Additionally, the seasonal patterns of the hygroscopic growth contribution to AOD are consistent across altitudes, with the highest values occurring in winter (0.82 in the BL, and 0.88 in the FT) and the lowest values in summer (0.66 in the BL, and 0.72 in the FT).

310 **Figure 8. Seasonal variations of 532-nm anthropogenic AOD_{amb}, AOD_{dry}, $\Delta AOD_{RH,BL}$, and $\Delta AOD_{RH,FT}$ in Wuhan during 2010-2024.**

4 Summary and Conclusions

In summary, we derive backscatter coefficient profiles of anthropogenic aerosols in the ambient atmosphere using ground-based polarization lidar observations over central China from 2010 to 2024. By combining these lidar-derived backscatter

315 profiles with EAR5 RH profiles, we further calculate the corresponding dry backscatter (and subsequently dry extinction) coefficient profiles by removing the contributions associated with hygroscopic growth. Our results reveal that hygroscopic growth of anthropogenic aerosols occurs primarily below 2 km. We find year-to-year particle backscatter enhancements ranging from 11% to 46%. The anthropogenic AOD in the ambient atmosphere ($AOD_{amb} = 0.404$) amplifies the dry anthropogenic AOD ($AOD_{dry} = 0.309$) by 30.7% via hygroscopic particle growth.

320 During China's rapid air-cleaning period of 2010–2017, anthropogenic aerosol emissions over central China decreased substantially, with AOD_{amb} exhibiting a rate of decline of -0.068 yr^{-1}. However, this rate does not accurately reflect the

actual improvement of atmospheric pollution, i.e., a rate of decline of -0.049 yr^{-1} which we derived from AOD_{dry}. The AOD contributed by hygroscopic growth, i.e., ΔAOD_{RH}, decreases rapidly from 2011 to 2013 and remains at a relatively low level thereafter. In addition, $\Delta AOD_{RH,BL}$ is generally 2-5 times larger than the corresponding $\Delta AOD_{RH,FT}$, which indicated a much

325 stronger contribution from aerosol hygroscopic growth within the BL, where most water vapor resides. Regarding the relative contributions of hygroscopic growth, both $\Delta AOD_{RH,BL}/AOD_{amb}$ and $\Delta AOD_{RH,FT}/AOD_{amb}$ exhibit the following features: (1) a marked decline during 2011-2014, due to effective mitigation of severe air pollution episodes and a concurrent shift toward a drier atmosphere as the result of changes of meteorological conditions over China; (2) a gradual increase during 2014-2019 (rising from 8% to 16% in the BL, and from 1% to 9% in the FT), influenced jointly by rising RH and a

330 growing proportion of more hydrophilic nitrate aerosols; (3) fluctuations at relatively high levels from 2020 onward (15-19% in the BL and 7-10% in the FT), as the upward trend associated with increasing RH is partially offset by a slight decline in the hygroscopic growth parameter γ since 2022. Furthermore, the seasonal variation of AOD_{amb} suggests that summer is the most polluted season, followed by autumn and winter. However, when removing hygroscopic growth effects, AOD_{dry} identifies that winter is in fact the peak pollution period over central China.

335 This study demonstrates that long-term ground-based observations combined with reanalysis meteorological data can capture the accurate variations in the atmospheric environment (air quality) through the derived dry AODs. This approach can also be extended from a single lidar site to regional, national, and even continental scales through established ground-based lidar networks, such as well-developed EARLINET in Europe (Pappalardo et al., 2014), MPLNET in the United States (Welton et al., 2001), and the recently developed CARLNET in China (Shao et al., 2025). In addition, AOD is a widely used

340 optical parameter in atmospheric science and can be further applied to derive key environmental metrics such as aerosol mass concentration (Shin et al., 2025). Achieving this will require reliable extinction-to-volume conversion factors, along with representative aerosol size distributions and densities (Mamouri and Ansmann, 2016; He et al., 2025). Such regional-specific pre-set aerosol information can be obtained from independent measurements, including sun photometers and optical particle counters. With these comprehensive observations and data processing methods, lidar observation holds strong

345 potential for monitoring three-dimensional variations of tropospheric pollution and improving aerosol reanalysis products as input constraints.

Data availability

ERA5 reanalysis data can be obtained from https://cds.climate.copernicus.eu/datasets (Copernicus Climate Change Service, Climate Data Store, 2025). The radiosonde data can be obtained from https://weather.uwyo.edu/upperair/sounding.shtml

350 (University of Wyoming Atmospheric Science Radiosonde Archive, 2025). Lidar data are available on reasonable request from the corresponding author (heyun@whu.edu.cn).

References

An, Z., Huang, R. J., Zhang, R., Tie, X., Li, G., Cao, J., Zhou, W., Shi, Z., Han, Y., Gu, Z., and Ji, Y.: Severe haze in northern China: A synergy of anthropogenic emissions and atmospheric processes, Proc. Natl Acad. Sci., 116, 8657–8666, https://doi.org/10.1073/pnas.190012511, 2019.

Bedoya-Velásquez, A. E., Navas-Guzmán, F., Granados-Muñoz, M. J., Titos, G., Román, R., Casquero-Vera, J. A., Ortiz Amezcua, P., Benavent-Oltra, J. A., de Arruda Moreira, G., Montilla-Rosero, E., Hoyos, C. D., Artiñano, B., Coz, E., Olmo-Reyes, F. J., Alados-Arboledas, L., and Guerrero-Rascado, J. L.: Hygroscopic growth study in the framework of EARLINET during the SLOPE I campaign: synergy of remote sensing and in situ instrumentation, Atmos. Chem. Phys., 18, 7001–7017, https://doi.org/10.5194/acp-18-7001-2018, 2018.

Bolton, D.: The computation of equivalent potential temperature, Mon. Weather. Rev., 108, 1046–1053, https://doi.org/10.1175/1520-0493(1980)108<1046:TCOEPT>2.0.CO;2, 1980.

Che, H., Zhang, X., Li, Y., Zhou, Z. and Qu, J.: Horizontal visibility trends in China 1981–2005, Geophys. Res. Lett., 34, L24706, https://doi.org/10.1029/2007GL031450, 2007.

Chen, J., Li, Z., Lv, M., Wang, Y., Wang, W., Zhang, Y., Wang, H., Yan, X., Sun, Y., and Cribb, M.: Aerosol hygroscopic
380   growth, contributing factors, and impact on haze events in a severely polluted region in northern China, Atmos. Chem. Phys., 19, 1327–1342, https://doi.org/10.5194/acp-19-1327-2019, 2019.

Chu, Q., Wang, Q., Feng, G., Jia, Z. and Liu, G. Roles of water vapor sources and transport in the intraseasonal and interannual variation in the peak monsoon rainfall over East China, Clim. Dyn., 57, 2153–2170, https://doi.org/10.1007/s00382-021-05799-5, 2021.

385   Copernicus Climate Change Service, Climate Data Store: ERA5 hourly data on from 1940 to present, Copernicus Climate Change Service (C3S) Climate Data Store (CDS), https://cds.climate.copernicus.eu/datasets (last access: 19 December 2025), 2025.

de Leeuw, G., Fan, C., Li, Z., Dong, J., Li, Y., Ou, Y., and Zhu, S.: Spatiotemporal variation and provincial scale differences of the AOD across China during 2000–2021, Atmos. Pollut. Res., 13, 101359,
390   https://doi.org/10.1016/j.apr.2022.101359, 2022.

Ding, A., Huang, X., Nie, W., Chi, X., Xu, Z., Zheng, L., Xu, Z., Xie, Y., Qi, X., Shen, Y., Sun, P., Wang, J., Wang, L., Sun, J., Yang, X.-Q., Qin, W., Zhang, X., Cheng, W., Liu, W., Pan, L., and Fu, C.: Significant reduction of $PM_{2.5}$ in eastern China due to regional-scale emission control: evidence from SORPES in 2011–2018, Atmos. Chem. Phys., 19, 11791–11801, https://doi.org/10.5194/acp-19-11791-2019, 2019.

395   Fernald, F. G.: Analysis of atmospheric lidar observations: some comments, Appl. Opt., 23, 652–653, https://doi.org/10.1364/AO.23.000652, 1984.

Ferrare, R. A., Melfi, S. H., Whiteman, D. N., Evans, K. D., Poellot, M., and Kaufman, Y. J.: Raman lidar measurements of aerosol extinction and backscattering: 2. Derivation of aerosol real refractive index, single-scattering albedo, and humidification factor using Raman lidar and aircraft size distribution measurements, J. Geophys. Res. Atmos., 10,
400   19673–19689, https://doi.org/10.1029/98JD01647, 1998.

Freudenthaler, V., Esselborn, M., Wiegner, M., Heese, B., Tesche, M., Ansmann, A., Müller, D., Althausen, D., Wirth, M., Fix, A., Ehret, G., Knippertz, P., Toledano, C., Gasteiger, J., Garhammer, M., and Seefeldner, M.: Depolarization ratio profiling at several wavelengths in pure Saharan dust during SAMUM2006, Tellus B, 61, 165–179, https://doi.org/10.1111/j.1600-0889.2008.00396.x, 2009.

405   Ganguly, D., Ginoux, P., Ramaswamy, V., Dubovik, O., Welton, J., Reid, E. A., and Holben, B. N.: Inferring the composition and concentration of aerosols by combining AERONET and MPLNET data: Comparison with other measurements and utilization to evaluate GCM output, J. Geophys. Res.-Atmos., 114, https://doi.org/10.1029/2009JD011895, 2009.

Geng, G., Liu, Y., Liu, Y., Liu, S., Cheng, J., Yan, L., Wu, N., Hu, H., Tong, D., Zheng, B., Yin, Z., He, K., and Zhang, Q.: Efficacy of China's clean air actions to tackle $PM_{2.5}$ pollution between 2013 and 2020, Nat. Geosci., 17, 987–994, https://doi.org/10.1038/s41561-024-01540-z, 2024.

Granados-Muñoz, M. J., Navas-Guzmán, F., Bravo-Aranda, J. A., Guerrero-Rascado, J. L., Lyamani, H., Valenzuela, A., Titos, G., Fernández-Gálvez, J., and Alados-Arboledas, L.: Hygroscopic growth of atmospheric aerosol particles based on active remote sensing and radiosounding measurements: selected cases in southeastern Spain, Atmos. Meas. Tech., 8, 705–718, https://doi.org/10.5194/amt-8-705-2015, 2015.

Guan, C., Wang, X., and Yang, H.: Understanding the development of the 2018/19 central Pacific El Niño, Adv. Atmos. Sci., 40, 177–185, https://doi.org/10.1007/s00376-022-1410-1, 2023.

Hänel, G.: The properties of atmospheric aerosol particles as functions of the relative humidity at thermodynamic equilibrium with the surrounding moist air, in: Advances in Geophysics, edited by: Landsberg, H. E. and Mieghem, J. V., Elsevier, 73–188, 1976.

He, Q., Gu, Y., and Zhang, M.: Spatiotemporal trends of $PM_{2.5}$ concentrations in central China from 2003 to 2018 based on MAIAC-derived high-resolution data, Environ. Int., 137, 105536, https://doi.org/10.1016/j.envint.2020.105536, 2020.

He, Y., Choudhury, G., Tesche, M., Ansmann, A., Yi, F., Müller, D., and Yin, Z.: Extended POLIPHON dust conversion factor dataset for lidar-derived cloud condensation nuclei and ice-nucleating particle concentration profiles, Atmos. Meas. Tech., 18, 5669–5685, https://doi.org/10.5194/amt-18-5669-2025, 2025.

He, Y., Jing, D., Yin, Z., Ohneiser, K., and Yi, F.: Long-term (2010–2021) lidar observations of stratospheric aerosols in Wuhan, China, Atmos. Chem. Phys., 24, 11431–11450, https://doi.org/10.5194/acp-24-11431-2024, 2024.

He, Y., Yi, F., Yi, Y., Liu, F., and Zhang, Y.: Heterogeneous nucleation of midlevel cloud layer influenced by transported Asian dust over Wuhan (30.5°N, 114.4°E), China, J. Geophys. Res.-Atmos., 126, e2020JD033394, https://doi.org/10.1029/2020JD033394, 2021.

Hersbach, H., Bell, B., Berrisford, P., Biavati, G., Horányi, A., Muñoz Sabater, J., Nicolas, J., Peubey, C., Radu, R., Rozum, I., Schepers, D., Simmons, A., Soci, C., Dee, D., Thépaut, J.-N.: ERA5 hourly data on pressure levels from 1940 to present, Copernicus Climate Change Service (C3S) Climate Data Store (CDS) [data set], https://doi.org/10.24381/cds.bd0915c6, 2023a.

Hersbach, H., Bell, B., Berrisford, P., Biavati, G., Horányi, A., Muñoz Sabater, J., Nicolas, J., Peubey, C., Radu, R., Rozum, I., Schepers, D., Simmons, A., Soci, C., Dee, D., and Thépaut, J.-N.: ERA5 hourly data on single levels from 1940 to present, Copernicus Climate Change Service (C3S) Climate Data Store (CDS) [data set], https://doi.org/10.24381/cds.adbb2d47, 2023b.

Jing, D., He, Y., Yin, Z., Liu, F., and Yi, F.: Long-term characteristics of dust aerosols over central China from 2010 to 2020 observed with polarization lidar. Atmos. Res., 297, 107129, https://doi.org/10.1016/j.atmosres.2023.107129, 2024.

Jing, D., He, Y., Yin, Z., Huang, K., Liu, F., and Yi, F.: Evolution of tropospheric aerosols over central China during 2010–2024 as observed by lidar, Atmos. Chem. Phys., 25, 17047–17067, https://doi.org/10.5194/acp-25-17047-2025, 2025a.

Jing, D., He, Y., Yin, Z., Müller, D., Huang, K., and Yi, F.: Hygroscopic growth characteristics of anthropogenic aerosols over central China revealed by lidar observations, EGUsphere [preprint], https://doi.org/10.5194/egusphere-2025-4965, 2025b.

445

Joo, S., Shin, J., Tesche, M., Dehkhoda, N., Kim, T., and Noh, Y.: Increased number concentrations of small particles explain perceived stagnation in air quality over Korea, Atmos. Chem. Phys., 25, 1023–1036, https://doi.org/10.5194/acp-25-1023-2025, 2025.

Kallihosur, T., Nair, V. S., and Sinha, P. R.: Winter haze amplification by aerosol hygroscopic growth over eastern Indo-Gangetic Plain, Commun. Earth Environ., 5, 656, https://doi.org/10.1038/s43247-024-01792-y, 2024.

450

Kong, W. and Yi, F.: Convective boundary layer evolution from lidar backscatter and its relationship with surface aerosol concentration at a location of a central China megacity, J. Geophys. Res.-Atmos, 120, 7928–7940, https://doi.org/10.1002/2015JD023248, 2015.

Li, C., van Donkelaar, A., Hammer, M. S., McDuffie, E. E., Burnett, R. T., Spadaro, J. V., Chatterjee, D., Cohen, A. J., Apte, J. S., Southerland, V. A., Anenberg, S. C., Brauer, M., and Martin, R. V.: Reversal of trends in global fine particulate matter air pollution, Nat. Commu., 14, 5349, https://doi.org/10.1038/s41467-023-41086-z, 2023.

455

Li, K., Zheng, F., Cheng, L., Zhang, T. and Zhu, J.: Record-breaking global temperature and crises with strong El Niño in 2023–2024, Innov. Geosci., 1, 100030, https://doi.org/10.59717/j.xinn-geo.2023.100030, 2023.

Liao, W., Zhou, J., Zhu, S., Xiao, A., Li, K., and Schauer, J. J.: Characterization of aerosol chemical composition and the reconstruction of light extinction coefficients during winter in Wuhan, China, Chemosphere, 241, 125033, https://doi.org/10.1016/j.chemosphere.2019.125033, 2020.

460

Liu, J., Ren, C., Huang, X., Nie, W., Wang, J., Sun, P., Chi, X., and Ding, A.: Increased aerosol extinction efficiency hinders visibility improvement in eastern China, Geophys. Res. Lett., 47, https://doi.org/10.1029/2020GL090167, 2020.

Liu, M., Huang, X., Song, Y., Xu, T., Wang, S., Wu, Z., Hu, M., Zhang, L., Zhang, Q., Pan, Y., Liu, X., and Zhu, T.: Rapid SO_2 emission reductions significantly increase tropospheric ammonia concentrations over the North China Plain, Atmos. Chem. Phys., 18, 17933–17943, https://doi.org/10.5194/acp-18-17933-2018, 2018.

465

Ma, Y., Zhang, M., Jin, S., Gong, W., Chen, N., Chen, Z., Jin, Y., and Shi, Y.: Long-term investigation of aerosol optical and radiative characteristics in a typical megacity of Central China during winter haze periods, J. Geophys. Res.-Atmos., 124, 12093–12106, https://doi.org/10.1029/2019JD030840, 2019.

470

Mamouri, R. E. and Ansmann, A.: Fine and coarse dust separation with polarization lidar, Atmos. Meas. Tech., 7, 3717–3735, https://doi.org/10.5194/amt-7-3717-2014, 2014.

Mamouri, R.-E. and Ansmann, A.: Potential of polarization lidar to provide profiles of CCN- and INP-relevant aerosol parameters, Atmos. Chem. Phys., 16, 5905–5931, https://doi.org/10.5194/acp-16-5905-2016, 2016.

Ministry of Ecology and Environment of the People's Republic of China: Technical guidelines for air pollution control projects, available at: https://www.mee.gov.cn/ywgz/fgbz/bz/bzwb/other/hjbhgc/201012/t20101224199112.shtml (last access: 18 December 2025), 2010 (in Chinese).

475

Miri, R., Pujol, O., Hu, Q., Goloub, P., Veselovskii, I., Podvin, T., and Ducos, F.: Innovative aerosol hygroscopic growth study from Mie–Raman–fluorescence lidar and microwave radiometer synergy, Atmos. Meas. Tech., 17, 3367–3375, https://doi.org/10.5194/amt-17-3367-2024, 2024.

480 Nair, V. S., Giorgi, F., and Keshav Hasyagar, U.: Amplification of South Asian haze by water vapour–aerosol interactions, Atmos. Chem. Phys., 20, 14457–14471, https://doi.org/10.5194/acp-20-14457-2020, 2020.

Navas-Guzmán, F., Martucci, G., Collaud Coen, M., Granados-Muñoz, M. J., Hervo, M., Sicard, M., and Haefele, A.: Characterization of aerosol hygroscopicity using Raman lidar measurements at the EARLINET station of Payerne, Atmos. Chem. Phys., 19, 11651–11668, https://doi.org/10.5194/acp-19-11651-2019, 2019.

485 Pappalardo, G., Amodeo, A., Apituley, A., Comeron, A., Freudenthaler, V., Linné, H., Ansmann, A., Bösenberg, J., D'Amico, G., Mattis, I., Mona, L., Wandinger, U., Amiridis, V., Alados-Arboledas, L., Nicolae, D., and Wiegner, M.: EARLINET: towards an advanced sustainable European aerosol lidar network, Atmos. Meas. Tech., 7, 2389–2409, https://doi.org/10.5194/amt-7-2389-2014, 2014.

Pérez-Ramírez, D., Whiteman, D. N., Veselovskii, I., Ferrare, R., Titos, G., Granados-Muñoz, M. J., Sánchez-Hernández, G.,
490 and Navas-Guzmán, F.: Spatiotemporal changes in aerosol properties by hygroscopic growth and impacts on radiative forcing and heating rates during DISCOVER-AQ 2011, Atmos. Chem. Phys., 21, 12021–12048, https://doi.org/10.5194/acp-21-12021-2021, 2021.

Shao, N., Wang, Q., Bu, Z., Yin, Z., Dai, Y., Chen, Y., and Wang, X.: China Aerosol Raman Lidar Network (CARLNET)— Part I: Water Vapor Raman Channel Calibration and Quality Control, Remote Sen., 17(3), 414,
495 https://doi.org/10.3390/rs17030414, 2025.

Shin, J., Sim, J., Tesche, M., Yoon, J., Kim, D., and Noh, Y.: Machine learning-based retrieval of aerosol size and hygroscopicity using horizontal scanning LiDAR and PM data, npj Clim. Atmos. Sci., https://doi.org/10.1038/s41612-025-01276-6, 2025.

Sicard, M., Fortunato dos Santos Oliveira, D. C., Muñoz-Porcar, C., Gil-Díaz, C., Comerón, A., Rodríguez-Gómez, A., and
500 Dios Otín, F.: Measurement report: Spectral and statistical analysis of aerosol hygroscopic growth from multi-wavelength lidar measurements in Barcelona, Spain, Atmos. Chem. Phys., 22, 7681–7697, https://doi.org/10.5194/acp-22-7681-2022, 2022.

Stoy, P. C., Roh, J., and Bromley, G. T.: It's the heat and the humidity: The complementary roles of temperature and specific humidity to recent changes in the energy content of the near-surface atmosphere, Geophys. Res. Lett., 49,
505 e2021GL096628, https://doi.org/10.1029/2021GL096628, 2022.

Tao, M., Chen, L., Xiong, X., Zhang, M., Ma, P., Tao, J., and Wang, Z.: Formation process of the widespread extreme haze pollution over northern China in January 2013: Implications for regional air quality and climate, Atmos. Environ., 98, 417–425, https://doi.org/10.1016/j.atmosenv.2014.09.026, 2014.

Tesche, M., Ansmann, A., Müller, D., Althausen, D., Engelmann, R., Freudenthaler, V., and Groß, S.: Vertically resolved
510   separation of dust and smoke over Cape Verde using multiwavelength Raman and polarization lidars during Saharan
       Mineral Dust Experiment 2008, J. Geophys. Res. Atmos., 114, D13202, https://doi.org/10.1029/2009JD011862, 2009.

Titos, G., Cazorla, A., Zieger, P., Andrews, E., Lyamani, H., Granados-Muñoz, M. J., Olmo, F. J., and Alados-Arboledas, L.:
       Effect of hygroscopic growth on the aerosol light-scattering coefficient: A review of measurements, techniques and
       error sources, Atmos. Environ., 141, 494–507, https://doi.org/10.1016/j.atmosenv.2016.07.021, 2016.

515 The State Council of the People's Republic of China: Action Plan on Air Pollution Prevention and Control, available at:
       https://www.gov.cn/zwgk/2013-09/12/content_2486773.html (last access: 18 December 2025), 2013 (in Chinese).

The State Council of the People's Republic of China: Three-year Plan on Defending the blue sky, available at:
       https://www.gov.cn/zhengce/content/2018-07-03/content_5303158.html (last access: 18 December 2025), 2018 (in
       Chinese).

520 The State Council of the People's Republic of China: Action Plan for continuous improvement of air quality, available at:
       https://www.gov.cn/gongbao/2023/issue_10886/202312/content_6921385.html (last access: 18 December 2025), 2023
       (in Chinese).

Toth, T. D., Zhang, J., Campbell, J. R., Reid, J. S., and Vaughan, M. A.: Temporal variability of aerosol optical thickness
       vertical   distribution   observed   from   CALIOP,   J.   Geophys.   Res.-Atmos.,   121,   9117–9139,
525   https://doi.org/10.1002/2015JD024668, 2016.

University of Wyoming Atmospheric Science Radiosonde Archive, https://weather.uwyo.edu/upperair/sounding.shtml, (last
       access: 19 December 2025), 2025.

Veselovskii, I., Whiteman, D. N., Kolgotin, A., Andrews, E. and Korenskii, M.: Demonstration of aerosol property profiling
       by multiwavelength lidar under varying relative humidity conditions, J. Atmos. Ocean. Tech. 26, 1543–1557,
530   https://doi.org/10.1175/2009JTECHA1254.1, 2009.

Wang, H., Tan, S. C., Wang, Y., Jiang, C., Shi, G. Y., Zhang, M. X., and Che, H. Z.: A multisource observation study of the
       severe prolonged regional haze episode over eastern China in January 2013, Atmos. Environ., 89, 807–815,
       https://doi.org/10.1016/j.atmosenv.2014.03.004, 2014.

Wang, K., Dickinson, R. and Liang, S: Clear sky visibility has decreased over land globally from 1973 to 2007, Science, 323,
535   1468–1470, https://doi.org/10.1126/science.1167549, 2009.

Wang, L. and Chen, W.: An intensity index for the East Asian winter monsoon, J. Climate, 27, 2361–2374,
       https://doi.org/10.1175/JCLI-D-13-00086.1, 2014.

Wang, X., Dickinson, R. E., Su, L., Zhou, C., and Wang, K.: $PM_{2.5}$ pollution in China and how it has been exacerbated by
       terrain and meteorological conditions, Bull. Am. Meteorol. Soc, 99, 105–119, https://doi.org/10.1175/BAMS-D-16-
540   0301.1, 2018.

Welton, E. J., Campbell, J. R., Spinhirne, J. D., and Scott III, V. S. (2001, February): Global monitoring of clouds and aerosols using a network of micropulse lidar systems, In Lidar remote sensing for industry and environment monitoring (Vol. 4153, pp. 151-158). SPIE.

Wu, B. and Wang, J.: Winter Arctic oscillation, Siberian high and East Asian winter monsoon, Geophys. Res. Lett., 29, 3–1, https://doi.org/10.1029/2002GL015373, 2002.

Wu, J., Luo, J., Zhang, L., Xia, L., Zhao, D., and Tang, J.: Improvement of aerosol optical depth retrieval using visibility data in China during the past 50 years, J. Geophys. Res.-Atmos, 119, 13–370, https://doi.org/10.1002/2014JD021550, 2016.

Xiao, X., Zhang, X., Xiao, Z., Liu, Z., Wang, D., Zhang, C., Rao, Z., He, X., and Guan, H.: Water vapor transport and its influence on water stable isotopes in the Dongting Lake basin, Atmos. Chem. Phys., 25, 6475–6496, https://doi.org/10.5194/acp-25-6475-2025, 2025.

Xu, W., Kuang, Y., Bian, Y., Liu, L., Li, F., Wang, Y., Xue, B., Luo, B., Huang, S., Yuan, B., Zhao, P., and Shao, M: Current challenges in visibility improvement in southern China, Environ. Sci. Technol. Lett., 7, 395–401, https://doi.org/10.1021/acs.estlett.0c00274, 2020.

Yao, L., Kong, S., Zheng, H., Chen, N., Zhu, B., Xu, K., Cao, W., Zhang, Y., Zheng, M., Cheng, Y., Hu, Y., Zhang, Z., Yan, Y., Liu, D., Zhao, T., Bai, Y., and Qi, S.: Co-benefits of reducing $PM_{2.5}$ and improving visibility by COVID-19 lockdown in Wuhan, npj Clim. Atmos. Sc., 4, 40, https://doi.org/10.1038/s41612-021-00195-6, 2021.

Yi, Y., Yi, F., Liu, F., Zhang, Y., Yu, C., and He, Y.: Microphysical process of precipitating hydrometeors from warm-front mid-level stratiform clouds revealed by ground-based lidar observations, Atmos. Chem. Phys., 21, 17649–17664, https://doi.org/10.5194/acp-21-17649-2021, 2021a.

Yi, Y., Yi, F., Liu, F., He, Y., Zhang, Y., and Yu, C.: A prolonged and widespread thin mid-level liquid cloud layer as observed by ground-based lidars, radiosonde and space-borne instruments, Atmos. Res., 263, 105815, https://doi.org/10.1029/2020JD033394, 2021b.

Yin, Z., Yi, F., Liu, F., He, Y., Zhang, Y., Yu, C., and Zhang, Y.: Long-term variations of aerosol optical properties over Wuhan with polarization lidar, Atmos. Environ., 259, 118508, https://doi.org/10.1016/j.atmosenv.2021.118508, 2021b.

Zhai, P., Yu, R., Guo, Y., Li, Q., Ren, X., Wang, Y., Xu, W., Liu, Y., and Ding, Y.: The strong El Niño of 2015/16 and its dominant impacts on global and China's climate, J. Meteorol. Res., 30, 283–297, https://doi.org/10.1007/s13351-016-6101-3, 2016.

Zhang, F., Wang, Z., Cheng, H., Lv, X., Gong, W., Wang, X., and Zhang, G.: Seasonal variations and chemical characteristics of $PM_{2.5}$ in Wuhan, central China, Sci. Total Environ., 518–519, 97–105, https://doi.org/10.1016/j.scitotenv.2015.02.054, 2015.

Zhang, Q., He, K., and Huo, H.: Cleaning China's air, Nature, 484, 161–162, https://doi.org/10.1038/484161a, 2012.

Zhang, Q., Zheng, Y., Tong, D., Shao, M., Wang, S., Zhang, Y., Xu, X., Wang, J., He, H., Liu, W., Ding, Y., Lei, Y., Li, J., Wang, Z., Zhang, X., Wang, Y., Cheng, j., Liu, Y., Shi, Q., Yan, L., Geng, G., Hong, C., Li, M., Liu, F., Zheng, B., Cao,

https://doi.org/10.5194/egusphere-2025-6360
Preprint. Discussion started: 4 January 2026
© Author(s) 2026. CC BY 4.0 License.

575   J., Ding, A., Gao, J., Fu, Q., Huo, J., Liu, B., Yang, F., He, K., and Hao, J.: Drivers of improved $PM_{2.5}$ air quality in China from 2013 to 2017, Proc. Natl. Acad. Sci., 116, 24463–24469, https://doi.org/10.1073/pnas.1907956116, 2019.

Zhang, Y., Zhang, Y., Yu, C., and Yi, F.: Evolution of aerosols in the atmospheric boundary layer and elevated layers during a severe, persistent haze episode in a central China megacity, Atmosphere, 12, 152, https://doi.org/10.3390/atmos12020152, 2021.

580   Zhao, G., Zhao, C., Kuang, Y., Tao, J., Tan, W., Bian, Y., Li, J., and Li, C.: Impact of aerosol hygroscopic growth on retrieving aerosol extinction coefficient profiles from elastic-backscatter lidar signals, Atmos. Chem. Phys., 17, 12133–12143, https://doi.org/10.5194/acp-17-12133-2017, 2017.

Zheng, B., Tong, D., Li, M., Liu, F., Hong, C., Geng, G., Li, H., Li, X., Peng, L., Qi, J., Yan, L., Zhang, Y., Zhao, H., Zheng, Y., He, K., and Zhang, Q.: Trends in China's anthropogenic emissions since 2010 as the consequence of clean air 585   actions, Atmos. Chem. Phys., 18, 14095–14111, https://doi.org/10.5194/acp-18-14095-2018, 2018.

Zheng, S., Pan, Y., Yu, L., Liu, S., and Peng, D.: Possible future movement of the Hu line based on IPCC CMIP6 scenarios, Environ. Res. Commun., 4, 095008, https://doi.org/10.1088/2515-7620/ac8c85, 2022.

Zhong, W., Wu, Y., Yang, S., Ma, T., Cai, Q., and Liu, Q.: Heavy Southern China spring rainfall promoted by multi-year El Niño events, Geophys. Res. Lett., 50, e2022GL102346, https://doi.org/10.1029/2022GL102346, 2023.